Article | Open Access

Energy Materials

Sheng *et al. Energy Mater.* **2026**, *6*, 600166 **DOI:**10.20517/energymater.2026.264

Confined iodine and accelerated redox kinetics enable high-rate Zn-iodine batteries

Fei Sheng[2], Mengxue Jin[2], Hedong Jiang[1,*], Dandan Huang[2], Pingchun Guo[2], Kailin Fu[1], Jiake Li[2], Xueguo Zhao[3], Hua Zhu[4], Yanxiang Wang[2,*]

Keywords:
Zinc-iodine batteries, graphene, high-rate performance, polyiodides

Citation: Sheng, F.; Jin, M.; Jiang, H.; Huang, D.; Guo, P.; Fu, K.; Li, J.; Zhao, X.; Zhu, H.; Wang, Y. Confined iodine and accelerated redox kinetics enable high-rate Zn-iodine batteries. *Energy Mater.* **2026**, *6*, 600166. https://dx.doi.org/10.20517/energymater.2026.264

Received: 6 Aug 2026
First Decision: 31 Aug 2026
Revised: 12 Oct 2026
Accepted: 23 Oct 2026
Published: 27 Nov 2026

Academic Editor:
Jiaqi Huang
Copy Editor:
Ping Zhang
Production Editor:
Ping Zhang

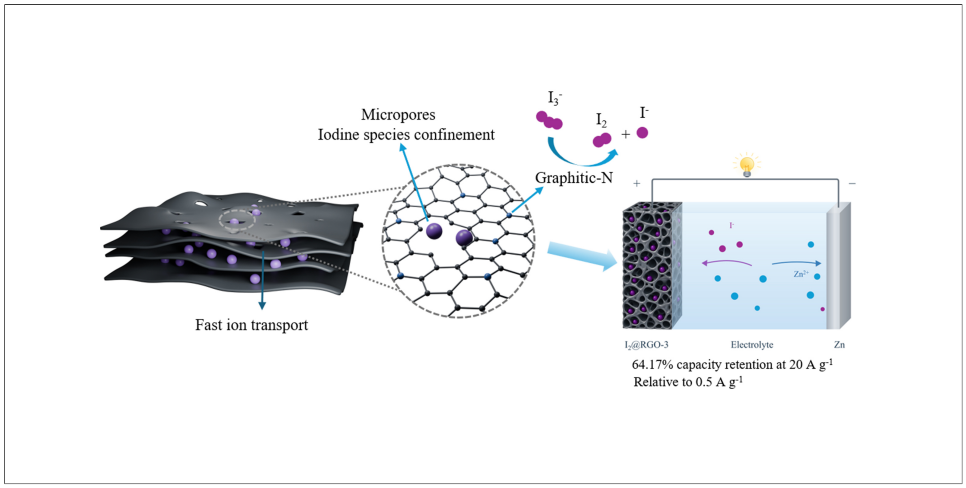

Abstract

Zinc-iodine batteries have attracted considerable attention owing to their high safety and low cost. However, their further development is hindered by the polyiodide shuttle effect and sluggish iodine redox kinetics. Here, we employed a synergistic strategy combining pore size regulation and nitrogen doping to design an iodine-loaded, nitrogen-doped reduced graphene oxide cathode (I_2@RGO-3) for enhanced iodine confinement and redox kinetics. The abundant microporous/mesoporous structure of the RGO framework physically confines electroactive iodine species, while the graphitic-N-rich interface facilitates interfacial charge transfer and promotes iodine redox kinetics. The as-prepared I_2@RGO-3 cathode demonstrates an outstanding rate capability, delivering a specific capacity of 172.23 mAh g^{-1} at 0.5 A g^{-1}, and even at a high current density of 20 A g^{-1}, it still retains 110.52 mAh g^{-1}, corresponding to a capacity retention of approximately 64.17%. It also exhibits stable cycling performance over 5,000 cycles. The synergistic strategy of pore size regulation and atomic doping proposed in this contribution provides new insights into the design of high-performance zinc-iodine battery cathodes.

[1]School of Energy Science and Engineering, Jingdezhen Ceramic University, Jingdezhen 333403, Jiangxi, China.
[2]School of Materials Science and Engineering, Jingdezhen Ceramic University, Jingdezhen 333403, Jiangxi, China.
[3]National Engineering Research Center for Domestic & Building Ceramics, Jingdezhen 333403, Jiangxi, China.
[4]School of Mechanical and Electrical Engineering, Jingdezhen Ceramic University, Jingdezhen 333403, Jiangxi, China.

***Correspondence to:** Dr. Hedong Jiang, School of Energy Science and Engineering, Jingdezhen Ceramic University, Jingdezhen 333403, Jiangxi, China. E-mail: 201003@jcu.edu.cn; Prof. Yanxiang Wang, School of Materials Science and Engineering, Jingdezhen Ceramic University, Jingdezhen 333403, Jiangxi, China. E-mail: wangyanxiang@jcu.edu.cn

INTRODUCTION

Among various electrochemical energy storage devices, aqueous zinc-iodine batteries (ZIBs) have attracted considerable attention for large-scale energy storage owing to their distinct advantages. First, Zn metal can be used in aqueous electrolytes over a broad pH range, from acidic to alkaline, and Zn-based rechargeable batteries can achieve a high Coulombic efficiency (CE) of over 90%. Additionally, Zn is abundant with global reserves of up to 1.9 billion tons, and it has a theoretical capacity of 820 mAh g^{-1}[1-3]. On the other hand, iodine, as the cathode material, also offers significant advantages, such as abundant reserves (with iodine content in seawater reaching approximately 55 μg per liter), a high theoretical capacity (211 mAh g^{-1} for the I_2/I^- reaction), and good reversibility and rapid redox kinetics[4-6]. These advantages make ZIBs a promising aqueous energy storage system.

Unlike conventional zinc-ion battery cathodes, which primarily store energy through solid-state ion intercalation/deintercalation, ZIBs mainly store energy through the reversible I^-/I_2 redox reaction for energy storage, accompanied by the interconversion of polyiodide intermediates (such as I_3^-)[7-9]. Under high-rate working conditions, the involvement of multiple phases and species places greater demands on reaction kinetics, as the reversible I^-/I_2 conversion must proceed within a shorter time frame. If this process is limited by I_2 dissolution and redeposition or by polyiodide diffusion in the electrolyte, the resulting kinetic and mass transport limitations can increase interfacial charge-transfer resistance and concentration polarization, thereby reducing the capacity at high rates. Therefore, the kinetics of the I^-/I_2 conversion and the mass transfer pathways of iodine species near the interface are the key controlling factors determining its high-rate performance[10-14].

In the process of reducing phase transformation resistance, polyiodide intermediates such as I_3^- exhibit a dual role. On the one hand, I_3^- can serve as an intermediate species between I^- and I_2, facilitating redox conversion through solution-phase polyiodide reactions and thereby alleviating the solid-liquid interfacial transport resistance associated with the direct involvement of crystalline I_2[15-17]. On the other hand, the high solubility and mobility of I_3^- facilitate its diffusion into the bulk electrolyte, which can lead to the loss of electroactive iodine and exacerbate the shuttle effect. Therefore, relying solely on strong adsorption or complete confinement strategies makes it difficult for iodine cathodes to balance rapid reaction kinetics with stable iodine retention at high rates[18-20]. Combining confinement within a porous framework with chemically active sites offers an effective strategy for enhancing iodine capture and retention[21]. Beyond iodine immobilization, accelerating the redox conversion of iodine species is also essential for achieving high-rate performance.

In recent years, researchers have increasingly focused on catalytic iodine cathode systems to address sluggish iodine redox kinetics. For instance, incorporating Fe single-atom sites into an ordered mesoporous conductive framework can simultaneously confine iodine species and catalyze the redox conversion[22]. The Ni single-atom-modified N-doped carbon material enhances polyiodide adsorption and promotes the reversible conversion of iodine species by regulating the electronic structure of the carbon matrix[23]. In addition, metal-coordinated molecular catalysts, such as hemin, have also been used to accelerate the conversion process of polyiodides[24].

Overall, constructing catalytic systems with well-defined metal active sites helps improve iodine redox kinetics and rate capability. However, such systems often require more complex structural design and synthesis procedures. The uniformity and stability of metal sites, together with structural evolution during long-term operation, must also be considered[25,26]. In contrast, metal-free carbon-based supports offer a simpler composition, good electrical conductivity, and lower cost. Defect-rich carbon and other metal-free

systems have demonstrated that rapid iodine conversion does not depend exclusively on metal catalytic sites[27-30]. For graphene-like supports, the key question is whether a simple hydrothermal approach to interfacial modulation can maintain the high reactivity of iodine species while limiting their excessive diffusion, thereby enabling high-rate iodine conversion.

Herein, hierarchically porous nitrogen-doped reduced graphene oxide (RGO) was prepared via a facile hydrothermal strategy using ammonia solution to regulate the pore architecture and interfacial chemistry. The optimized RGO-3 host combines accessible microporous and mesoporous channels with a graphitic-N-rich interface, helping immobilize iodine and polyiodide species while facilitating ion transport and interfacial redox reactions. This work examines the coupled effects of pore structure and N-containing surface chemistry on polyiodide confinement, mass transport, and interfacial charge transfer. Collectively, these effects improve the rate capability and cycling stability of ZIBs.

EXPERIMENTAL

Preparation of RGO film

Firstly, the graphene oxide (GO) suspension was prepared by the modified Hummers method. Then, a 10 mg mL^{-1} GO suspension was evenly coated on polytetrafluoroethylene (PTFE) plate to obtain the GO film after being dried at room temperature. Subsequently, the GO film that had been cut was completely immersed in the solvent to proceed with the hydrothermal reaction (180 °C for 6 h). Finally, the RGO films were obtained. The samples obtained from different solvents (the ratio of ammonia solution to water is 0%, 30%, 70%, 100%) were labeled as RGO-0, RGO-3, RGO-7, and RGO-10.

Assembly of zinc-I_2 Battery

The hydrothermally reduced RGO films were placed in the saturated iodine solution and soaked for 24 h to obtain the I_2@RGO cathode films (the corresponding electrode parameters are listed in Supplementary Table 1). Mixed cellulose ester filters (Shanghai Xingya Purification Material Factory) and a pure Zn sheet (Qinghe County Tengfeng Metal Materials Co., Ltd.) were used as the separator and anode, respectively. The electrolyte was prepared by dissolving 2 M $Zn(CF_3SO_3)_2$ [analytical reagent grade (AR), Sinopharm Chemical Reagent Co., Ltd.], 0.1 M ZnI_2 (AR, Sinopharm Group Chemical Reagent Co.) and 0.5 wt% sodium carboxymethyl cellulose (CMC-Na) (AR, Sinopharm Group Chemical Reagent Co.) in deionized water.

Material characterization and electrochemical measurements

The surface and cross-sectional microstructures of the prepared materials were observed using a scanning electron microscope (SEM, SU8010, Hitachi). The elemental composition and content of the materials were also determined by this instrument. An X-ray diffraction analyzer (XRD, Bruker, D8-Advance A25) was used to characterize the phase and crystal plane characteristics of the materials. The elemental composition and defect state and graphitization degree of the materials were analyzed in detail by X-ray photoelectron spectroscopy (XPS, Thermo Scientific K-Alpha) and a laser Raman spectrometer (Raman, WITec alpha300R). The specific surface area and pore size distribution of the samples were precisely characterized by the nitrogen adsorption-desorption method and Barrett-Joyner-Halenda (BJH) model. The thermal stability of the samples was tested under an argon atmosphere with a heating rate of 10 °C min^{-1} using the thermogravimetric analysis (TGA). The adsorption ability of the samples for iodine was analyzed through an ultraviolet-visible spectrophotometer (UV-5500). Electrochemical characterization was performed on an electrochemical workstation (CHI660E). Cyclic voltammetry (CV) curves were recorded with a potential range from 0.2 to 1.8 V at various scan rates. Galvanostatic charge-discharge (GCD) curves were measured with the current density from 0.5 to 20 A g^{-1}. Electrochemical impedance spectroscopy (EIS) measurements covered frequencies from 0.01 Hz to 100 kHz at the open-circuit potential with a 5 mV alternating current perturbation. Cycling stability was assessed at 10 A g^{-1} for 5000 charging-discharging cycles on a Neware

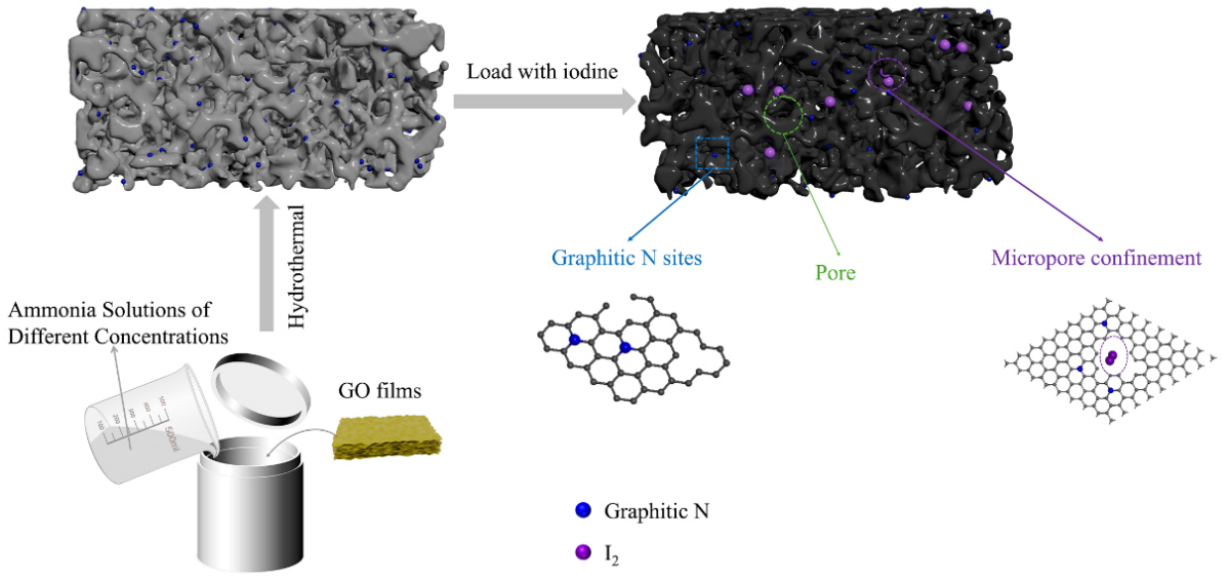

Figure 1. Schematic illustration of the fabrication process and proposed working mechanism of the I_2@RGO cathodes. GO: Graphene oxide; RGO: reduced graphene oxide.

BTS-4000.

RESULTS AND DISCUSSION

As illustrated in Figure 1, adjusting the volume fraction of ammonia solution in the hydrothermal system enables the simultaneous regulation of nitrogen incorporation and pore evolution within the RGO framework. During hydrothermal treatment, the GO films are reduced and reconstructed into a nitrogen-doped porous RGO architecture, followed by iodine loading to form the I_2@RGO cathode. The resulting structure serves several complementary functions. The graphitic-N-rich interface facilitates interfacial charge transfer and contributes to improved iodine redox kinetics. Meanwhile, the interconnected pore network, particularly the mesoporous channels, shortens ion-transport pathways and thus supports high-rate operation. More importantly, the micropores physically confine iodine species and reduce their diffusion into the electrolyte, thereby mitigating polyiodide shuttling and active-material loss. The combined effects of graphitic-N catalysis, rapid ion transport, and micropore confinement contribute to the enhanced reaction kinetics, rate performance, and cycling stability of the I_2@RGO cathodes.

Effect of ammonia concentration on RGO materials

Figure 2 shows the cross-sectional SEM images of RGO films prepared with different ammonia/water ratios. As the proportion of ammonia solution increases, the RGO films evolve from a loose, porous network into a more densely stacked layered structure. When pure water is used as the solvent, the oxygen-containing functional groups (OFGs) on the graphene surface are removed during the hydrothermal reduction process, and the interplay between electrostatic repulsion and van der Waals forces leads to the formation of a porous network [Figure 2A and E]. When the volume fraction of ammonia solution in the mixed solvent increases to 30%, the carboxyl group (-COOH) on the GO sheets can deprotonate to form $-COO^-$ groups. NH_4^+ ions promote bridging these groups and partially screen the electrostatic repulsion between the sheets[31,32], resulting in a more uniform and compact interlayer pore structure [Figure 2B and F]. However, when undiluted ammonia solution is used, the degree of carboxyl group ionization on the graphene sheets decreases, weakening interlayer electrostatic repulsion. This will further result in the van der Waals forces remaining the dominant microforces in the GO systems, which contributes to the aggregation and stacking [Figure 2D and H].

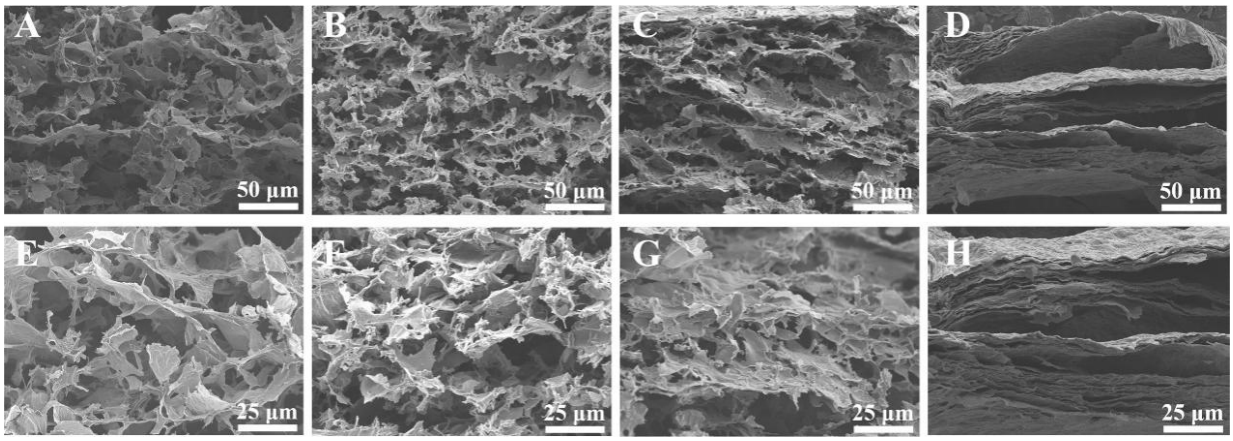

Figure 2. Cross-sectional SEM images of (A and E) RGO-0; (B and F) RGO-3; (C and G) RGO-7; (D and H) RGO-10. SEM: Scanning electron microscope; RGO: reduced graphene oxide.

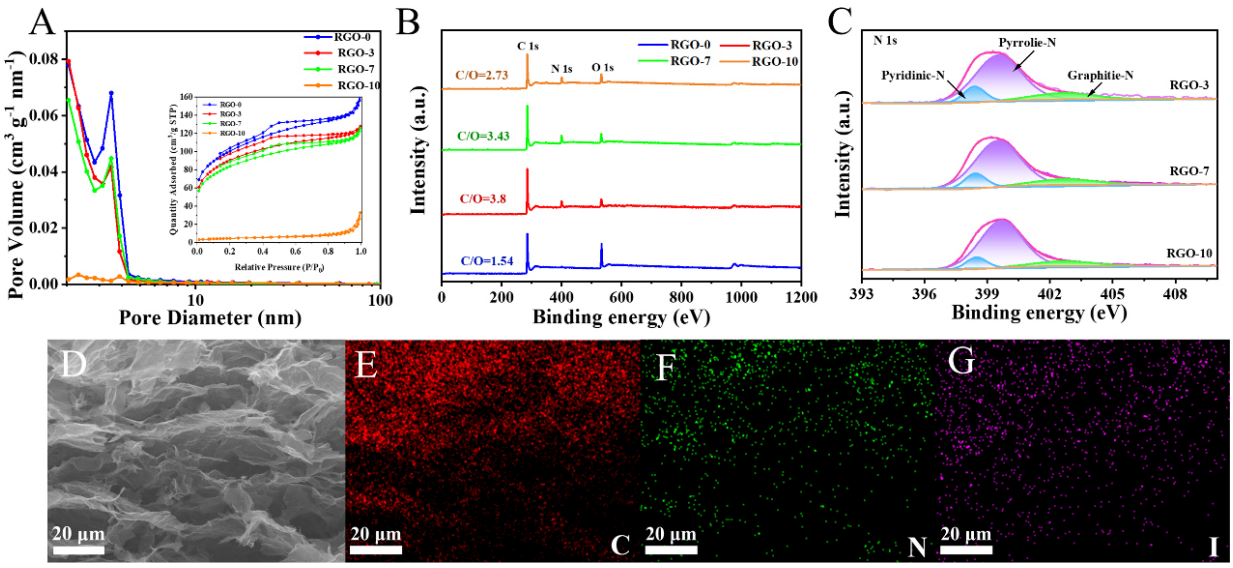

Figure 3. (A) Pore size distributions of RGO-0, RGO-3, RGO-7, and RGO-10 (inset: corresponding N_2 adsorption-desorption isotherms); (B) XPS spectra of the four samples; (C) N 1s spectra of RGO-3, RGO-7 and RGO-10; (D) SEM images of the I_2@RGO-3 section; elemental mapping of I_2@RGO-3: (E) C; (F) N; (G) I. RGO: Reduced graphene oxide; XPS: X-ray photoelectron spectroscopy; SEM: scanning electron microscope.

Nitrogen adsorption-desorption measurements were performed to investigate the specific surface area (SSA) and pore size distribution of the RGO samples. All four samples exhibit type IV isotherms, indicating a hierarchical porous characteristic [Figure 3A]. When the relative pressure (P/P_0) is within the range of 0-0.2, the rapid increase in adsorption amount indicates the presence of micropores in the material[33]. Moreover, the lagging ring formed by the curve in the range of 0.2-0.9 reflects the existence of the mesoporous structure inside the material, and the larger the area of the lagging ring, the more mesopore volume there is[34]. These features suggest that RGO-0, RGO-3, and RGO-7 possess a combination of micropores and mesopores, whereas these characteristics are less pronounced in RGO-10. Based on the Brunauer-Emmett-Teller (BET) method, the SSA of the four samples RGO-0, RGO-3, RGO-7, and RGO-10 are 354.21, 320.26, 295.11, and 15.64 $m^2 g^{-1}$, respectively. Furthermore, the pore-size distributions derived from the BJH model further confirm that RGO-0, RGO-3, and RGO-7 possess hierarchical micro/mesoporous structures. Such a hierarchical porous architecture provides abundant confinement spaces and accessible channels for iodine adsorption[35].

Figure 3B shows the XPS spectra of the four RGO samples. All samples exhibit distinct peaks at 284.8 eV and 534.08 eV, assigned to C 1s and O 1s, respectively. Additionally, N 1s peaks are observed at 399.9 eV in RGO-3, RGO-7, and RGO-10, supporting the incorporation of nitrogen into RGO during hydrothermal treatment in the presence of ammonia. Further, Figure 3C shows the N 1s spectra of the three samples, which all consist of pyridine nitrogen (398.38 eV), pyrrole nitrogen (399.68 eV), and graphitic nitrogen (402.88 eV). Based on the integrated peak areas, graphitic N accounts for 13.69% of the total N 1s peak area in RGO-3, higher than the corresponding proportions in RGO-7 (12.25%) and RGO-10 (11.4%). In general, nitrogen-containing functional groups can interact strongly with iodine, thereby enhancing iodine adsorption by the electrode material[36]. In addition, graphitic N sites contribute to accelerating the redox conversion of iodine species, suggesting that RGO-3 is a promising host for iodine immobilization. Supplementary Figure 1 exhibits the C 1s spectrum of RGO-3, mainly composed of C-C/C=C peaks (284.8 eV), C-N peaks (285.58 eV), C-O peaks (286.68 eV), C=O peaks (287.78 eV), and O-C=O peaks (289.38 eV). The appearance of the C-N peak provides further evidence for the successful doping of the N element. Supplementary Figure 2 displays the O 1s spectrum of RGO-3, mainly containing C=O (531.08 eV), C-O/C-OH (532.58 eV), and COOH (533.88 eV) peaks. The C=O component accounts for the largest proportion of the O 1s peak area. These groups could also contribute additional charge storage through the formation of C-O-Zn bonds during electrochemical cycling[37].

As shown in Supplementary Figure 3, the energy-dispersive X-ray spectroscopy (EDS) element mapping images show that C, O and N are distributed throughout the cross-section of RGO-3, supporting the presence of nitrogen within the material. Figure 3D-G and Supplementary Figure 4 present the cross-sectional SEM image and corresponding EDS elemental mappings of I_2@RGO-3. The electrode retains a fluffy and interconnected three-dimensional porous structure. The C, N, I and O signals are detected throughout the cross-sectional area, indicating that iodine is well incorporated within the RGO-3 framework. This observation is consistent with the above XPS results.

To verify the existence of the iodine form in RGO-3, XRD was conducted. From Figure 4A, both patterns display a relatively broad diffraction peak at around 24°, corresponding to the (002) crystal plane of graphitic carbon. When RGO-3 adsorbs iodine, the corresponding diffraction peak slightly weakens and no crystalline iodine peak is observed, demonstrating that the iodine adsorbed in the I_2@RGO-3 is in the molecular state. Subsequently, Raman tests were conducted on RGO-3 and I_2@RGO-3 to explore the influence of adsorbed iodine on the defect degree of the graphene matrix [Supplementary Figure 5]. The intensity ratio of the D band to the G band (I_D/I_G) increases from 0.999 for RGO-3 to 1.049 for I_2@RGO-3, suggesting a slight increase in structural disorder, which can be attributed to the interaction between iodine species and the carbon framework[38].

The XPS survey spectra in Figure 4B show characteristic peaks for both samples at binding energies of 284.8 eV, 399.9 eV and 534.08 eV, corresponding to C 1s, N 1s and O 1s, respectively. The N 1s signal further supports nitrogen incorporation into RGO-3 during hydrothermal treatment with aqueous ammonia. In addition, typical characteristic peaks (I $3d_{3/2}$ peaks at 630 and 632.0 eV and the I $3d_{5/2}$ peaks at 618.6 and 620.5 eV) of I 3d were detected in I_2@RGO-3, implying that iodine does not react chemically with RGO-3 during the adsorption period. The high-resolution I 3d spectra in Figure 4C show no clearly resolved components assigned to iodide (I^-) or polyiodide anions (I_3^- and I_5^-). These results are consistent with iodine being predominantly present in molecular form within RGO-3[39].

TGA was used to evaluate iodine loading and thermal retention in RGO-3. As shown in Figure 4D, I_2 began to lose mass at approximately 130 °C and was completely volatilized by approximately 187 °C, which was mainly caused by the sublimation of I_2[40]. RGO-3 and I_2@RGO-3 showed slight mass loss of 11.59 wt% and

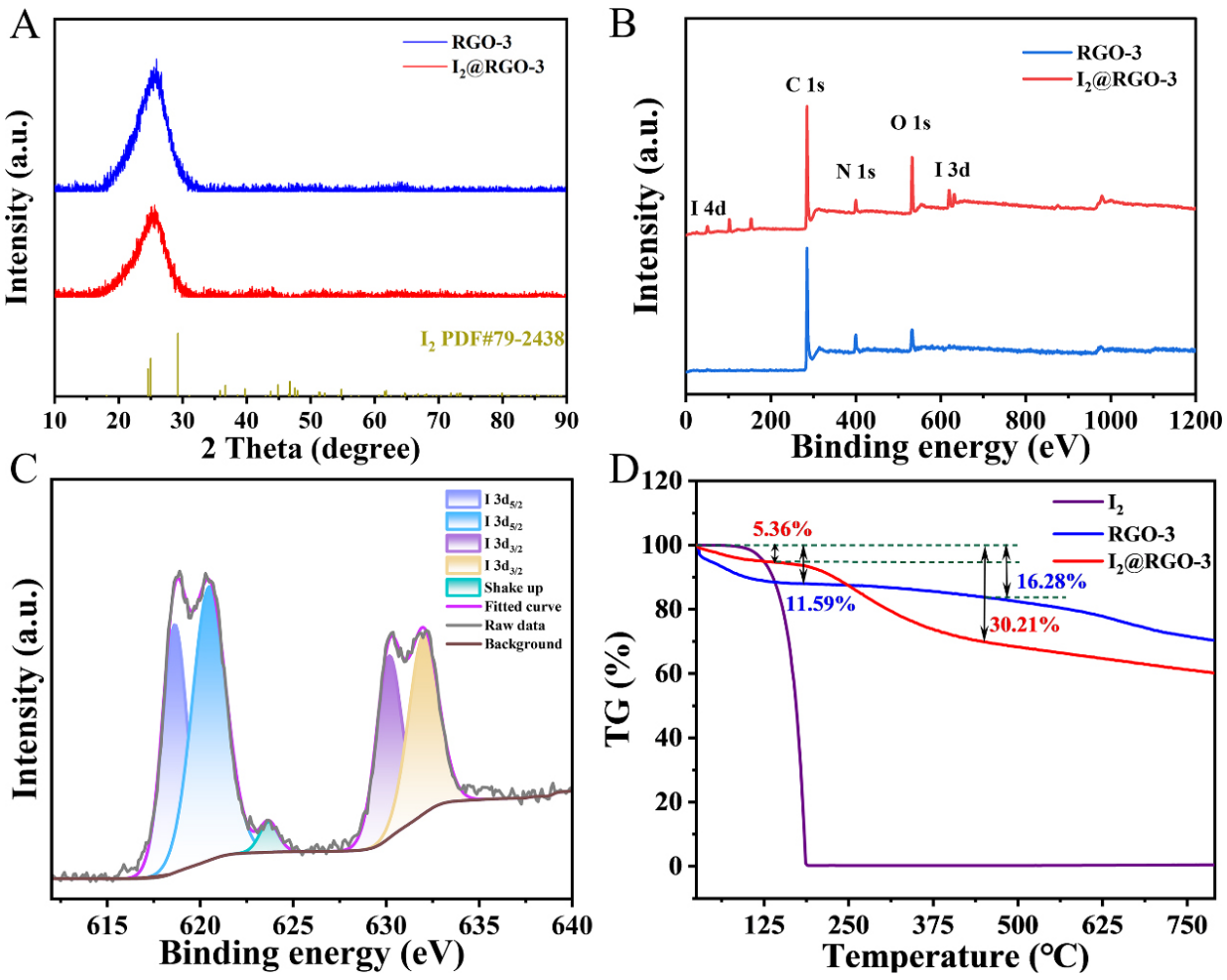

Figure 4. (A) XRD patterns, (B) Total XPS spectra of RGO-3 and I_2@RGO-3; (C) I 3d spectrum of I_2@RGO-3; (D) TGA curves for I_2, RGO-3 and I_2@RGO-3; the annotated percentages represent cumulative weight losses from 25 °C to the indicated temperatures. XRD: X-ray diffraction; XPS: X-ray photoelectron spectroscopy; RGO: reduced graphene oxide; TG: thermogravimetry; TGA: thermogravimetric analysis; PDF: powder diffraction file.

5.36 wt%, respectively, upon heating to approximately 140 °C. This was mainly due to the presence of the OFGs on the surfaces of both samples, and these OFGs were hydrophilic and could adsorb water from the ambient atmosphere. As the temperature increased, the water adsorbed by both samples was volatilized and some OFGs were decomposed, resulting in a certain amount of mass loss for both samples[41]. The cumulative weight losses of I_2@RGO-3 and RGO-3 from 25 °C to approximately 450 °C were 30.21 wt% and 16.28 wt%, respectively. After subtracting their respective cumulative weight losses up to approximately 140 °C, the additional losses over 140-450 °C were 24.85 wt% and 4.69 wt%, respectively. Subtracting the RGO-3 background loss over this interval gave an estimated iodine loading of 20.16 wt%.

Visual adsorption experiments were conducted to investigate iodine uptake by RGO-3. Supplementary Figure 6 shows the color change of the solution when placing RGO-3 in a saturated iodine solution. The saturated iodine solution appears dark brown initially. As a comparison, in the solution with the RGO-3 electrode, the color of the solution gradually turns light brown in 120 h, indicating that RGO-3 can adsorb iodine dissolved in the solution. Ultraviolet-visible (UV-vis) spectra were collected at different time intervals to further evaluate the adsorption behavior. As shown in Supplementary Figure 7, the reference iodine solution without RGO-3 exhibits an absorption band at approximately 450 nm, assigned to I_2, accompanied by the characteristic absorption bands of I_3^- at approximately 290 and 350-355 nm[42-44]. Meanwhile, after

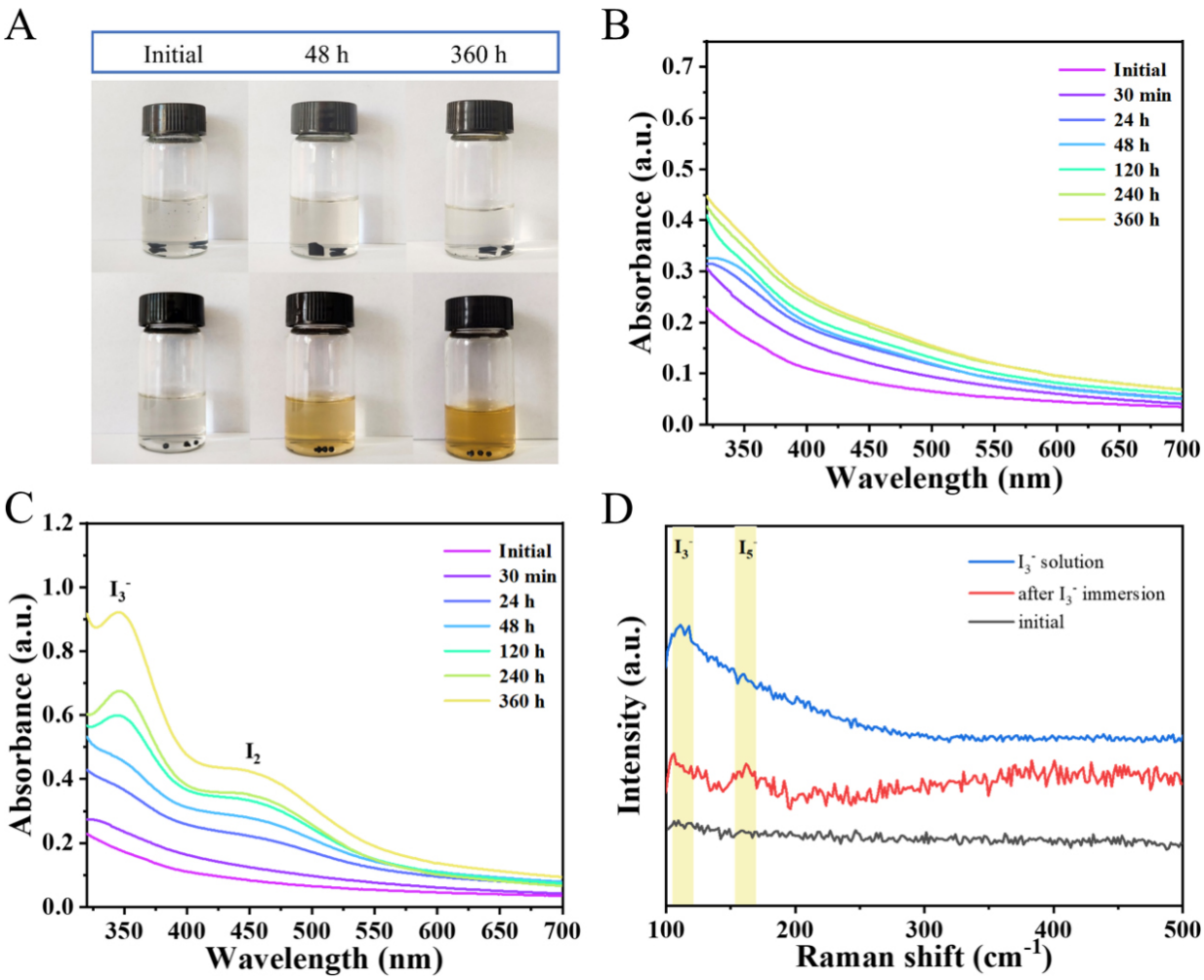

Figure 5. (A) Optical photographs of electrolytes containing I_2@RGO-3 (top row) and pure I_2 (bottom row) at selected immersion times (0, 48, and 360 h). The complete time series is provided in Supplementary Figure 8 (Photographs taken by the authors). UV-vis spectra of the electrolyte after immersion of (B) I_2@RGO-3 and (C) pristine I_2; (D) Raman spectra of the initial RGO-3 electrode, triiodide solution, and RGO-3 electrode after immersion in the triiodide solution for 12 h. RGO: Reduced graphene oxide; UV-vis: ultraviolet-visible.

adding the RGO-3 sample, the absorption peak of I_2 significantly weakens, and the peak of I_3^- also slightly decreases, verifying that RGO-3 has a significant adsorption effect on iodine, which is consistent with the optical photos of RGO-3 adsorbing iodine mentioned above.

Furthermore, I_2@RGO-3 and I_2 were respectively immersed in the electrolyte solution to study the ability of RGO-3 to anchor iodine. As shown in Figure 5A and Supplementary Figure 8, the electrolyte containing pure I_2 gradually changed from colorless to dark brown over 360 h as iodine dissolved into the electrolyte. By contrast, the electrolyte containing I_2@RGO-3 remained nearly colorless throughout the immersion test, indicating that the RGO-3 host effectively suppressed the release of iodine species into the electrolyte[45]. UV-vis spectra of the electrolytes were also collected at different time intervals to further assess iodine retention by RGO-3. As shown in Figure 5B and C, after adding I_2 to the electrolyte solution, the absorption peaks of I_3^- and I_2 gradually became more obvious over time, reflecting the progressive dissolution of iodine in the electrolyte. In contrast, these bands were barely detectable in the electrolyte containing I_2@RGO-3 throughout the 360 h immersion period, further supporting the ability of RGO-3 to retain iodine species and suppress their release into the electrolyte.

To further investigate the interaction between polyiodides and RGO, Raman spectra were collected before and after immersing the RGO electrodes in a triiodide-containing solution for 12 h. As shown in Figure 5D, the initial RGO electrode shows no obvious iodine-related Raman feature, whereas a weak band at approximately 110 cm^{-1} appears after immersion, which can be assigned to an I_3^--related vibration. An additional weak feature around 160 cm^{-1} is also observed after adsorption, possibly originating from higher-order polyiodide species stabilized at the RGO interface. Together with the decrease in I_3^- absorbance in the residual solutions measured by UV-vis spectroscopy, these results support the adsorption and immobilization of soluble polyiodides by the RGO framework.

To further evaluate the ability of RGO to immobilize soluble polyiodide species, static adsorption experiments were carried out using the same polyiodide solution. As shown in Supplementary Figure 9, the initial solution exhibited characteristic absorption bands at approximately 290 and 350 nm, assigned to I_3^- species. After 12 h of contact with the RGO electrodes, the intensity of these absorption bands decreased significantly, indicating that the soluble polyiodides were immobilized by the RGO electrodes. Among the samples studied, RGO-3 produced the lowest residual absorbance, the most effective polyiodide removal under the tested conditions. This ability to retain soluble polyiodide intermediates could help limit their migration into the bulk electrolyte and mitigate the shuttle effect.

Electrochemical performance tests of the I_2@RGO-3//Zn battery

The CV curves of the four I_2@RGO//Zn cells were recorded over a voltage window of 0.2-1.8 V, as shown in Figure 6A. At a scan rate of 2 mV s^{-1}, all curves showed obvious redox peaks between 1.2-1.4 V, corresponding to the redox process of I_2/I^-. Notably, I_2@RGO-3 shows a relatively narrow overall redox potential span compared with I_2@RGO-0, I_2@RGO-7, and I_2@RGO-10. The relatively smaller potential span of I_2@RGO-3 suggests lower overall electrochemical polarization during the iodine redox process[46]. Figure 6B displays the GCD curves of the four samples at 1 A g^{-1}. Consistent with the redox features observed in the CV curves, I_2@RGO-3 shows the longest charging-discharging plateau near 1.2-1.3 V. In addition, the charging and discharging curves of I_2@RGO-3 also show a smaller voltage gap (ΔE), indicating higher reversibility. It can be seen from Figure 6C that the specific capacities of the four samples at 0.5 A g^{-1} are 158.26, 172.23, 141.02 and 135.78 mAh g^{-1}, respectively. When the current density increases to 20 A g^{-1}, the specific capacities of I_2@RGO-0, I_2@RGO-3, I_2@RGO-7 and I_2@RGO-10 are 92.79, 110.52, 90.01, and 36.11 mAh g^{-1}, respectively. The discharge specific capacity of I_2@RGO-3 remains 64.17% of the original capacity when the current density increases by 40 times, higher than that of other electrode materials I_2@RGO-0 (58.63%), I_2@RGO-7 (63.83%), and I_2@RGO-10 (26.59%). Moreover, to further demonstrate the superiority of the present design, the rate performance of I_2@RGO-3 was compared with those of previously reported iodine-based electrodes in Figure 6D[47-56]. The I_2@RGO-3 electrode exhibits an excellent retention rate over a wide current-density range, retaining 64.17% of its capacity even at 20 A g^{-1}. As shown in the Nyquist plots of the four samples in Supplementary Figure 10, the I_2@RGO-3 electrode exhibits the lowest charge-transfer resistance (R_{ct}), suggesting facilitated interfacial charge transfer. The smaller redox potential separation, reduced charge-discharge voltage hysteresis, and lower charge-transfer resistance consistently demonstrate the more favorable iodine redox kinetics of I_2@RGO-3. Therefore, I_2@RGO-3 is the optimum electrode when used as the cathode in ZIBs. To further study the electrochemical kinetics of the I_2@RGO-3 material, the CV curves at different scan rates ranging from 2 to 50 mV s^{-1} were measured [Figure 6E].

$$i = k_1 v + k_2 v^{1/2} \quad (1)$$

where i is the measured current at a given potential, v is the scan rate, $k_1 v$ represents the capacitive-controlled current contribution, and $k_2 v^{1/2}$ represents the diffusion-controlled current contribution. k_1 and k_2 are the corresponding constants.

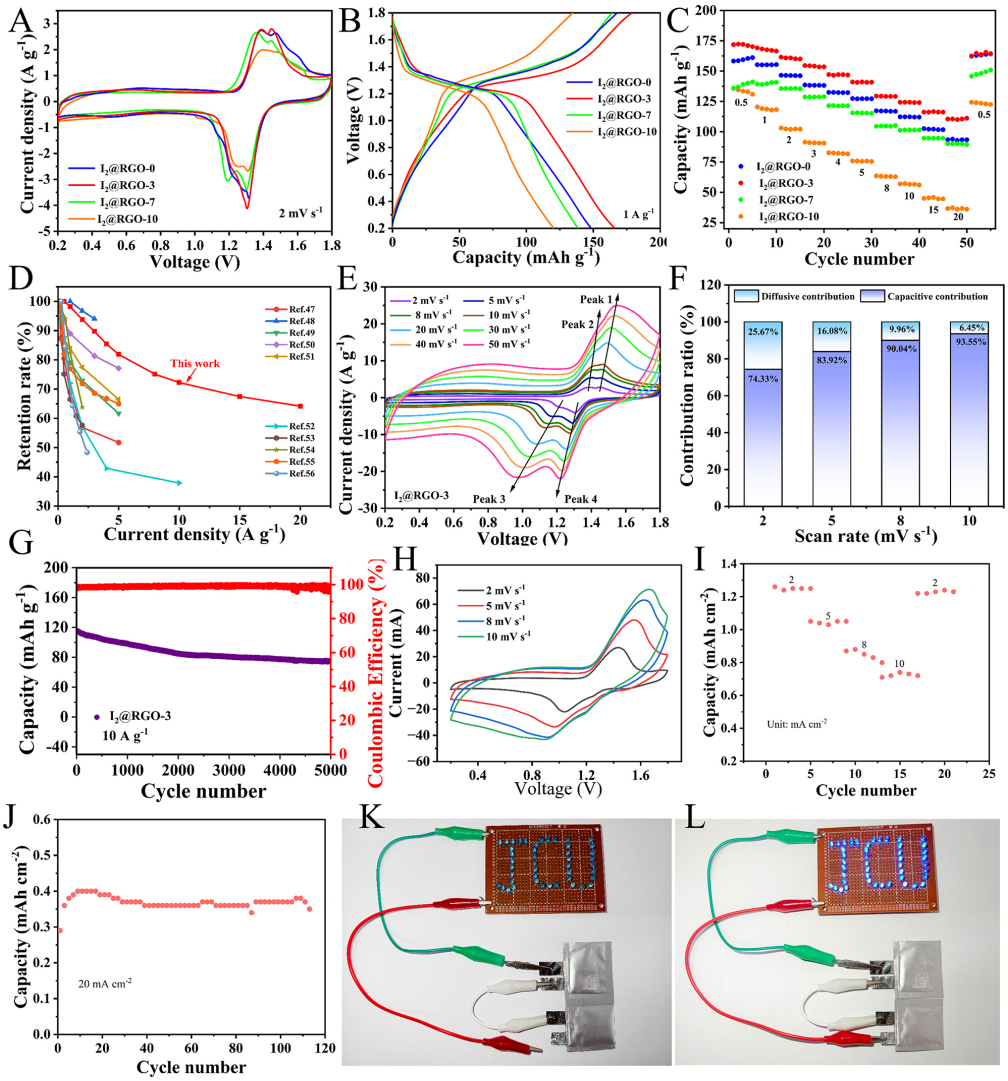

Figure 6. (A) CV curves at 2 mV s^{-1}, (B) GCD curves at 1 A g^{-1}, and (C) rate performance of the I_2@RGO-0, I_2@RGO-3, I_2@RGO-7, and I_2@RGO-10 electrodes; (D) comparison of the rate capability of I_2@RGO-3 with that of previously reported iodine-based electrodes[47-56]. The corresponding literature data are summarized in Supplementary Table 2; (E) CV curves at different scan rates of 2-50 mV s^{-1} of I_2@RGO-3//Zn batteries; (F) Capacitance contribution diagram at 2-10 mV s^{-1}; (G) Long-term cycling performance of I_2@RGO-3//Zn; Electrochemical performance and LED demonstration of Zn-I_2 pouch cells using the I_2@RGO-3 cathode; (H) CV curves at scan rates of 2, 5, 8, and 10 mV s^{-1}; (I) Rate performance of the pouch cell at current densities applied in the following sequence: 2 ⟶ 5 ⟶ 8 ⟶ 10 ⟶ 2 mA cm^{-2}; (J) Cycling performance at 20 mA cm^{-2}; (K and L) Photographs of two pouch cells connected in series to power an LED array, with the LEDs off and on, respectively (Photographs taken by the authors). CV: Cyclic voltammetry; GCD: galvanostatic charge-discharge; RGO: reduced graphene oxide; LED: light-emitting diode.

Based on the peak current of the CV curve and the scan rate, formula (1) was used to draw the capacitance contribution graph of the I_2@RGO-3 electrode. When the scan rate was 2 mV s^{-1}, the capacitance contribution rate of the I_2@RGO-3 electrode was 74.33%. As the scan rate gradually increased to 10 mV s^{-1}, the contribution rate of charge capacitance to the total capacity gradually increased to 83.92%, 90.04% and 93.55% for 5 mV s^{-1}, 8 mV s^{-1} and 10 mV s^{-1}, respectively, as displayed in Figure 6F and Supplementary Figure 11. Such dominant capacitive behavior in I_2@RGO-3 indicates rapid charge/discharge kinetics, directly correlating with its superior rate capability and cycling stability. Furthermore, to verify the interconversion among I^-, I_3^-, and I_2, *ex situ* Raman spectra were collected at selected points along the charge-discharge curve [Supplementary Figure 12A and B].

Cycling stability and CE are important indicators of battery performance. As shown in Figure 6G, ZIBs using I_2@RGO-3 as the cathode exhibit stable cycling over 5,000 cycles at a current density of 10 A g^{-1}. The average capacity decay per cycle is only 0.007%, and the average CE is as high as 98.98%, demonstrating cycling stability and high charge-discharge efficiency. This performance can be partly attributed to pore confinement within the nitrogen-doped RGO-3 host, which helps retain iodine species and suppress their dissolution and polyiodide shuttling. Subsequently, SEM characterization analysis was conducted on the I_2@RGO-3 electrode materials before and after 1,000 cycles, as shown in Supplementary Figure 13. The surface of the I_2@RGO-3 electrode material before cycling presented a fluffy, porous structure. Due to the compression caused by the assembly of the battery, the SEM image showed that the surface of the I_2@RGO-3 material was dense, the elemental distribution map also shows that iodine remains after cycling. This indicates that the I_2@RGO-3 material has a good adsorption capacity for the iodine species, and can restrict the iodine species in the microporous structure of the I_2@RGO-3 material.

To evaluate the applicability of the I_2@RGO-3 cathode, Zn-I_2 pouch cells were assembled. As shown in Figure 6H, the CV curves exhibit similar profiles at scan rates of 2-10 mV s^{-1}, with slight shifts in the redox peak potentials as the scan rate increases. Figure 6I presents the rate performance of the pouch cell. As the current density increases from 2 to 10 mA cm^{-2}, the discharge capacity gradually decreases with increasing electrode polarization. The cell delivers an areal capacity of 1.25 mAh cm^{-2} at 2 mA cm^{-2} and retains 0.74 mAh cm^{-2} at 10 mA cm^{-2}, corresponding to a capacity retention of 59.2%. These results show that the I_2@RGO-3 cathode maintains its high-rate charge-discharge capability in the pouch-cell configuration. When the current density returns from 10 to 2 mA cm^{-2}, the capacity recovers to 1.23 mAh cm^{-2}, indicating good capacity recovery after the rate test. During cycling at 20 mA cm^{-2}, the discharge capacity initially increases from approximately 0.30 to 0.40 mAh cm^{-2} during activation and subsequently decreases to approximately 0.35 mAh cm^{-2} at the 113th cycle, corresponding to a capacity retention of 87.5% relative to the post-activation capacity of 0.40 mAh cm^{-2} [Figure 6J]. Two pouch cells connected in series successfully power a light-emitting diode (LED) array, producing a clear blue letter pattern [Figure 6K and L] and demonstrating their ability to supply power to a small electronic device.

CONCLUSION

In summary, nitrogen-doped RGO hosts with tunable pore architectures and nitrogen configurations were constructed for Zn-I_2 batteries. The results clarify the respective roles of pore architecture and nitrogen configuration in addressing the two major challenges of iodine cathodes. The hierarchical micro/mesoporous structure of RGO-3 provides physical confinement for iodine-active species and suppresses polyiodide-related shuttling, while the graphitic-N-rich interface promotes interfacial charge transfer and facilitates more favorable iodine redox kinetics. These structural and interfacial characteristics enable I_2@RGO-3 to deliver 172.23 mAh g^{-1} at 0.5 A g^{-1} and retain 64.17% of its capacity at 20 A g^{-1}. Overall, the results establish the distinct contributions of pore architecture and nitrogen configuration to iodine confinement and redox kinetics, providing a mechanistic basis for the design of RGO-based cathode hosts for Zn-I_2 batteries.

DECLARATIONS

Authors' contributions

Writing-original draft, methodology, formal analysis, visualization: Sheng, F.
Methodology, investigation: Jin, M.
Writing-review & editing, methodology, funding acquisition, conceptualization: Jiang, H.
Visualization, funding acquisition: Huang, D.
Formal analysis: Guo, P.
Methodology: Fu, K.; Zhao, X.; Zhu, H.
Resources: Li, J.
Writing-review & editing, resources, methodology: Wang, Y.

Availability of data and materials

The original contributions presented in this study are included in the article/Supplementary Materials. Further inquiries can be directed to the corresponding authors.

AI and AI-assisted tools statement

During the preparation of this manuscript, the AI tool DeepSeek (version V4.1-Flash, released 2026-09-10) was used solely for language editing. Doubao (version Seed 2.1 Lite, released 2026-09-23) was used to generate the cathode illustration within the zinc-iodine battery schematic in the Graphical Abstract (GA). This illustration is intended solely for conceptual visualization and does not represent experimentally measured morphology or quantitative data. These tools did not influence the study design, data collection, analysis, interpretation, or the scientific content of the work. All authors take full responsibility for the accuracy, integrity, and final content of the manuscript.

Financial support and sponsorship

The authors gratefully acknowledge the financial support from the Science and Technology Research Project of Jiangxi Province Education Department (GJJ2500906), Social Development Project of Jingdezhen Science and Technology Bureau (2026SF009), and the Doctoral Scientific Research Foundation of Jingdezhen Ceramic University (No. 102-01003002060).

Conflicts of interest

All authors declared that there are no conflicts of interest.

Ethical approval and consent to participate

Not applicable.

Consent for publication

Not applicable.

Copyright

© The Author(s) 2026.

Supplementary Materials

Supplementary Materials

REFERENCES

1. Qin, L.; Zhou, J.; Sun, M.; et al. Comprehensive review for zinc powder anodes: significance, optimizing design, and industrial feasibility in zinc-ion batteries. *Energy. Storage. Mater.* **2025**, *74*, 103917. DOI
2. Li, Y.; Ma, L.; Xu, W.; et al. Strong adsorption FeNC catalytic cathode for 50,000 cycles aqueous zinc-iodine batteries. *J. Colloid. Interface. Sci.* **2025**, *679*, 893-905. DOI
3. Bian, H.; Wang, C.; Wang, Y.; et al. Phase inversion-induced porous polymer coating for high rate and stable zinc anode. *Adv. Funct. Mater.* **2024**, *34*, 2401760. DOI
4. Yang, H.; Qiao, Y.; Chang, Z.; Deng, H.; He, P.; Zhou, H. A metal-organic framework as a multifunctional ionic sieve membrane for long-life aqueous zinc-iodide batteries. *Adv. Mater.* **2020**, *32*, e2004240. DOI
5. Zong, W.; Li, J.; Zhang, C.; et al. Dynamical janus interface design for reversible and fast-charging zinc-iodine battery under extreme operating conditions. *J. Am. Chem. Soc.* **2024**, *146*, 21377-88. DOI
6. Wu, J.; Yang, J.; Zhang, B.; Fan, H. J. Immobilizing polyiodides with expanded Zn^{2+} channels for high-rate practical zinc-iodine battery. *Adv. Energy. Mater.* **2024**, *14*, 2302738. DOI
7. Xu, Z.; Yang, J.; Sun, P.; et al. Iodide-mediated intermediate regulation strategy enables high-capacity and ultra-stable zinc-iodine batteries. *Chem. Sci.* **2025**, *16*, 13211-20. DOI
8. Liu, Y.; Zhou, K.; Wang, R.; et al. $I^+/I^2/I^-$ conversion toward energy-dense aqueous Zn-I_2 batteries: progress and perspective. *Chem. Sci.* **2025**, *16*, 16381-91. DOI
9. Liu, T.; Wang, H.; Lei, C.; et al. Recognition of the catalytic activities of graphitic N for zinc-iodine batteries. *Energy. Storage. Mater.* **2022**, *53*, 544-51. DOI

10. Wang, Y.; Cui, Y.; Zhao, M.; et al. Zwitterion-mediated interface chemistry for practical Zn-iodine batteries. *Nat. Commun.* **2025**, *16*, 5565. DOI PubMed PMC
11. Zhang, Y.; Ali, U.; Hao, Y.; et al. Anchoring polyiodide with flexible interlayer for high-performance aqueous zinc-iodine batteries. *J. Colloid. Interface. Sci.* **2025**, *688*, 132-9. DOI
12. Zhang, L.; Zhang, M.; Guo, H.; et al. A universal polyiodide regulation using quaternization engineering toward high value-added and ultra-stable zinc-iodine batteries. *Adv. Sci.* **2022**, *9*, e2105598. DOI
13. Xu, H.; Zhang, R.; Luo, D.; et al. Polarity coupling in biphasic electrolytes enables iodine/polyiodide co-extraction for portable Zn-iodine batteries following a liquid-liquid conversion route. *Energy. Environ. Sci.* **2025**, *18*, 7447-59. DOI
14. Lin, P.; Chen, G.; Kang, Y.; et al. Simultaneous inhibition of Zn dendrites and polyiodide ions shuttle effect by an anion concentrated electrolyte membrane for long lifespan aqueous zinc-iodine batteries. *ACS. Nano.* **2023**, *17*, 15492-503. DOI
15. Zhu, J.; Ni, J.; Li, L. Harnessing in situ iodine ionic liquids for high areal capacity and long cycle life Zn//I_2 solid microbatteries. *Adv. Funct. Mater.* **2025**, *35*, 2416799. DOI
16. Ke, J.; Bai, K.; Zhang, Z.; et al. Enabling I_3^-/I_2 redox couple toward high-voltage Zn-polyiodide batteries by the iodide-π conjugation effect. *ACS. Nano.* **2025**, *19*, 17746-59. DOI
17. Chang, X.; Cabot, A. Insights on Polyidide Shuttling of Zn-I_2 batteries by I_3^-/I^- electrolytes based on the dual-ion battery system. *Nanomaterials* **2025**, *15*, 738. DOI PubMed PMC
18. Jiang, X.; Wang, Y.; Li, W.; et al. High-performance Zn-I_2 batteries enabled by porous hetero-carbon nanofiber hosts with TiO_2 homojunctions. *Adv. Fiber. Mater.* **2026**, *8*, 87-98. DOI
19. Du, W.; Miao, L.; Song, Z.; et al. Organic iodine electrolyte starting triple I^+ storage in In-based metal-organic frameworks for high-capacity aqueous Zn-I_2 batteries. *Chem. Eng. J.* **2024**, *484*, 149535. DOI
20. Chen, Z.; Gao, X.; Shan, L.; et al. Taming polyiodides: phenol chemistry for shuttle-free and durable zinc–iodine batteries. *Energy. Environ. Sci.* **2025**, *18*, 8768-79. DOI
21. Guo, P.; Wu, Y.; Ma, X.; et al. Enhanced iodine capture by nano-copper particles modified benzimidazole-based molded porous carbon. *Appl. Surf. Sci.* **2025**, *708*, 163754. DOI
22. Yang, X.; Fan, H.; Hu, F.; Chen, S.; Yan, K.; Ma, L. Aqueous zinc batteries with ultra-fast redox kinetics and high iodine utilization enabled by iron single atom catalysts. *Nano-Micro. Lett.* **2023**, *15*, 126. DOI PubMed PMC
23. Lee, J.; Lee, W.; Back, S.; et al. Activating iodine redox by enabling single-atom coordination to dormant nitrogen sites to realize durable zinc-iodine batteries. *EES. Catal.* **2024**, *2*, 276-85. DOI
24. Chen, Z.; Wang, F.; Ma, R.; et al. Molecular catalysis enables fast polyiodide conversion for exceptionally long-life zinc-iodine batteries. *ACS. Energy. Lett.* **2024**, *9*, 2858-66. DOI
25. Liu, Y.; Zhang, W. Large-scale synthesis of functional single-atom catalysts. *Commun. Chem.* **2023**, *6*, 36. DOI PubMed PMC
26. Zhang, L.; Yang, J.; Yang, X.; Wang, A.; Zhang, T. Structural evolution of single-atom catalysts. *Chem. Catal.* **2023**, *3*, 100560. DOI
27. Zhang, P.; Li, J.; Zhang, S.; et al. Toward shuttle-free Zn-I_2 battery: anchoring and catalyzing iodine conversion by high-density P-doping sites in carbon host. *Adv. Funct. Mater.* **2024**, *34*, 2306359. DOI
28. Wang, W.; Li, R.; Xu, X.; et al. Electrocatalysts in zinc-iodine batteries: theoretical insights and material design. *Coord. Chem. Rev.* **2025**, *544*, 216951. DOI
29. Niu, S.; Zhao, B.; Liu, D. High-performance Zn-I_2 batteries enabled by a metal-free defect-rich carbon cathode catalyst. *ACS. Appl. Mater. Interfaces.* **2023**, *15*, 25558-66. DOI
30. Sun, M.; Wei, L.; Li, X.; et al. Highly stable aqueous Zn-I_2 batteries enabled by the synergistic adsorption/conversion effect via porous graphitic iodine host. *Colloids. Surf. A. Physicochem. Eng. Asp.* **2024**, *703*, 135330. DOI
31. Lu, Y.; Huang, L.; Guo, Y.; Yang, X. Theoretical insights into origin of graphene oxide acidity and relating behavior of oxygen-containing groups in water. *Carbon* **2021**, *183*, 355-61. DOI
32. Wang, Q. J.; Sun, H. J.; Peng, T. J.; Feng, M. Z. Structure development during the cation-exchange processes of graphite oxide. *Acta. Phys. Chim. Sin.* **2017**, *33*, 413-8. DOI
33. Lu, F.; Liu, C.; Zhang, X.; et al. Study on full-scale pores characterization and heterogeneity of coal based on low-temperature nitrogen adsorption and low-field nuclear magnetic resonance experiments. *Sci. Rep.* **2024**, *14*, 16910. DOI PubMed PMC
34. Li, Z.; Turner, J.; Snurr, R. Q. Computational investigation of hysteresis and phase equilibria of n-alkanes in a metal-organic framework with both micropores and mesopores. *Commun. Chem.* **2023**, *6*, 90. DOI PubMed PMC
35. Fu, W.; Hu, G.; Song, W.; Dou, M.; Wang, F. Nitrogen-doped hierarchically porous carbon derived from biomass for efficient capture of iodine. *Appl. Surf. Sci.* **2025**, *682*, 161664. DOI

36. Liu, X.; Yuan, H.; Zheng, Q.; et al. Understanding the adsorption sites on nitrogen- and oxygen-doped carbon nanotubes for iodine uptake. *Appl. Surf. Sci.* **2023**, *629*, 157387. DOI
37. Jiang, H.; Zhang, Y.; Sheng, F.; et al. Graphene film with a controllable microstructure for efficient electrochemical energy storage. *Appl. Mater. Interfaces.* **2023**, *15*, 13086-96. DOI
38. Fitzek, H.; Sterrer, M.; Knez, D.; et al. Impact of iodine electrodeposition on nanoporous carbon electrode determined by EQCM, XPS and in situ raman spectroscopy. *Nanomaterials* **2023**, *13*, 1545. DOI PubMed PMC
39. Li, H.; Zhang, D.; Cheng, K.; Li, Z.; Li, P. Effective iodine adsorption by nitrogen-rich nanoporous covalent organic frameworks. *ACS. Appl. Nano. Mater.* **2023**, *6*, 1295-302. DOI
40. Shang, W.; Li, Q.; Jiang, F.; et al. Boosting Zn||I_2 battery's performance by coating a zeolite-based cation-exchange protecting layer. *Nano-Micro. Lett.* **2022**, *14*, 82. DOI PubMed PMC
41. Singh, S. B.; Dastgheib, S. A. Physicochemical transformation of graphene oxide during heat treatment at 110-200 °C. *Carbon. Trends.* **2023**, *10*, 100251. DOI
42. Aluker, N. L.; Herrmann, M. Spectrophotometric analysis of iodine forms in solutions of iodine compounds. *Opt. Spectrosc.* **2021**, *129*, 599-604. DOI
43. Yue, Q.; Wan, Y.; Li, X.; et al. Restraining the shuttle effect of polyiodides and modulating the deposition of zinc ions to enhance the cycle lifespan of aqueous Zn-I_2 batteries. *Chem. Sci.* **2024**, *15*, 5711-22. DOI
44. Wei, Z.; Wang, Y.; Hong, H.; et al. Long-life aqueous zinc-iodine flow batteries enabled by selectively intercepting hydrated ions. *Nat. Commun.* **2025**, *16*, 9301. DOI PubMed PMC
45. Bai, C.; Cai, F.; Wang, L.; Guo, S.; Liu, X.; Yuan, Z. A sustainable aqueous Zn-I_2 battery. *Nano. Res.* **2018**, *11*, 3548-54. DOI
46. Cao, S.; Zhang, A.; Fang, H.; et al. Skin-like quasi-solid-state electrolytes for spontaneous zinc-ion dehydration toward ultra-stable zinc-iodine batteries. *Energy. Environ. Sci.* **2025**, *18*, 3395-406. DOI
47. Fu, Y.; Zhu, L.; Zheng, X.; et al. Enhanced adsorption-catalytic conversion of iodine species by amorphous CoP@C host materials for zinc iodine battery. *Chem. Bio. Eng.* **2025**, *2*, 341-9. DOI PubMed PMC
48. Chen, M.; Zhu, W.; Guo, H.; et al. Tightly confined iodine in surface-oxidized carbon matrix toward dual-mechanism zinc-iodine batteries. *Energy. Storage. Mater.* **2023**, *59*, 102760. DOI
49. Wu, Y.; Qian, Y.; Huang, C.; et al. Hierarchical porous soft carbon host for the cathode of an aqueous zinc-iodine battery with ultra-long cycle life. *Electrochim. Acta.* **2023**, *460*, 142593. DOI
50. Guo, Q.; Wang, H.; Sun, X.; Yang, Y.; Chen, N.; Qu, L. In situ synthesis of cathode materials for aqueous high-rate and durable Zn-I_2 batteries. *ACS. Materials. Lett.* **2022**, *4*, 1872-81. DOI
51. Zhang, Y.; Wang, L.; Li, Q.; et al. Iodine promoted ultralow Zn nucleation overpotential and Zn-rich cathode for low-cost, fast-production and high-energy density anode-free Zn-iodine batteries. *NanoMicro. Lett.* **2022**, *14*, 208. DOI PubMed PMC
52. Zhang, S. J.; Hao, J.; Li, H.; et al. Polyiodide confinement by starch enables shuttle-free Zn-iodine batteries. *Adv. Mater.* **2022**, *34*, e2201716. DOI
53. Wei, F.; Xu, H.; Zhang, T.; et al. Mesoporous poly(3,4-ethylenedioxythiophene):poly(styrenesulfonate) as efficient iodine host for high-performance zinc-iodine batteries. *ACS. Nano.* **2023**, *17*, 20643-53. DOI
54. Yu, Z.; Gong, Z.; Wen, R.; et al. Gelatinized starch as a low-cost and bifunctional binder enables shuttle-free aqueous zinc-iodine batteries. *Rare. Met.* **2024**, *43*, 6351-61. DOI
55. Zhao, Y.; Wang, Y.; Xue, W.; et al. Unveiling the role of cationic pyridine sites in covalent triazine framework for boosting zinc-iodine batteries performance. *Adv. Mater.* **2024**, *36*, e2403097. DOI
56. Zeng, X.; Meng, X.; Jiang, W.; et al. Anchoring polyiodide to conductive polymers as cathode for high-performance aqueous zinc-iodine batteries. *ACS. Sustain. Chem. Eng.* **2020**, *8*, 14280-5. DOI

Disclaimer/Publisher's Note: All statements, opinions, and data contained in this publication are solely those of the individual author(s) and contributor(s) and do not necessarily reflect those of OAE and/or the editor(s). OAE and/or the editor(s) disclaim any responsibility for harm to persons or property resulting from the use of any ideas, methods, instructions, or products mentioned in the content.

© The Author(s) 2026. Open Access This article is licensed under a Creative Commons Attribution 4.0 International License (https://creativecommons.org/licenses/by/4.0/), which permits unrestricted use, sharing, adaptation, distribution and reproduction in any medium or format, for any purpose, even commercially, as long as you give appropriate credit to the original author(s) and the source, provide a link to the Creative Commons license, and indicate if changes were made.